Biochimica et Biophysica Acta 1838 (2014) 2615–2624

Contents lists available at ScienceDirect

Biochimica et Biophysica Acta

journal homepage: www.elsevier.com/locate/bbamem

The dynamics of giant unilamellar vesicle oxidation probed by morphological transitions

Shalene Sankhagowit [a], Shao-Hua Wu [b], Roshni Biswas [b], Carson T. Riche [a], Michelle L. Povinelli [b], Noah Malmstadt [a,*]

[a] Mork Family Department of Chemical Engineering and Materials Science, University of Southern California, Los Angeles, CA 90089-1211, USA
[b] Ming Hsieh Department of Electrical Engineering, University of Southern California, Los Angeles, CA 90089-2560, USA

ARTICLE INFO

Article history:
Received 15 March 2014
Received in revised form 21 June 2014
Accepted 24 June 2014
Available online 3 July 2014

Keywords:
Lipid oxidation
Lipid peroxidation
Phospholipid tail scission
Oxidation kinetic
Giant unilamellar vesicle
Membrane pore

ABSTRACT

We have studied the dynamics of Lissamine Rhodamine B dye sensitization-induced oxidation of 1,2-dioleoyl-sn-glycero-3-phosphocholine (DOPC) giant unilamellar vesicles (GUVs), where the progression of the underlying chemical processes was followed via vesicle membrane area changes. The surface-area-to-volume ratio of our spherical GUVs increased after as little as ten seconds of irradiation. The membrane area expansion was coupled with high amplitude fluctuations not typical of GUVs in isoosmotic conditions. To accurately measure the area of deformed and fluctuating membranes, we utilized a dual-beam optical trap (DBOT) to stretch GUV membranes into a geometrically regular shape. Further oxidation led to vesicle contraction, and the GUVs became tense, with micron-scale pores forming in the bilayer. We analyzed the GUV morphological behaviors as two consecutive rate-limiting steps. We also considered the effects of altering DOPC and 1,2-dipalmitoyl-sn-glycero-3-phosphoethanolamine-N-(lissamine rhodamine B sulfonyl) (RhDPPE) concentrations. The resulting kinetic model allows us to measure how lipid molecular area changes during oxidation, as well as to determine the rate constants controlling how quickly oxidation products are formed. Controlled membrane oxidation leading to permeabilization is also a potential tool for drug delivery based on engineered photosensitizer-containing lipid vesicles.

1. Introduction

Lipid bilayer membranes are the structural barriers that set boundaries of the cell and its compartments. They serve as the platforms on which membrane proteins are localized and play a central role in a host of physiological processes. The ability of lipid bilayers to perform their physiological role depends on the integrity of the membrane structure [1]. Lipid oxidation causes modification and/or loss of essential membrane functions [2] and has been identified in pathological conditions such as cancer [3,4] and aging-associated conditions such as atherosclerosis [5] and Alzheimer's disease [6]. Despite the strong connection of membrane oxidation to human health, the specific molecular mechanisms connecting lipid oxidation to the membrane's roles in disease etiology and pathogenesis are not well understood. Here, we use a light-induced model of lipid oxidation to probe the kinetics of lipid oxidation by observing oxidation-linked changes to the morphology of giant unilamellar lipid vesicles (GUVs).

The key oxidation process that occurs within the lipid bilayer involves oxidative species such as reactive oxygen species (ROS) attacking unsaturated lipids. The products of the oxidation reactions depend on the type of lipids involved (including mono- and polyunsaturated) and the particular oxidative species mediating the attack [7]. However, the most commonly observed fundamental process can be viewed as a series of key chemical events. First, the oxidation of an unsaturated lipid molecule is initiated by the abstraction of the allylic hydrogen adjacent to the double bond and the reaction with molecular oxygen to form a carbon-centered peroxyl radical. This in turns initiates the oxidation of neighboring lipid molecules, and the lipid tails are left modified with a hydroperoxy group [8,9], and further oxidation leads to lipid tail scission into a truncated lipid molecule and tail fragment [10].

Singlet oxygen ($^1O_2$) is an ROS frequently encountered during the visualization of the lipid membrane by fluorescence microscopy. When irradiated, photosensitive molecules such as porphyrin derivatives and fluorescent rhodamine dyes can transfer their energy to molecular oxygen (O_2) to generate the more reactive $^1O_2$ [11,12]. Biomedically, single oxygen production by photosensitization is utilized by photodynamic therapy (PDT) for targeted destruction of malignant tissues [13]. Singlet oxygen is also naturally-occurring, resulting when UVA rays photosensitize endogenous porphyrins [14].

Singlet oxygen-induced effects have been noted to alter membrane phase behavior [15,16]. Other reports have noted more drastic changes to the lipid membrane morphology induced by singlet oxygen-related

* Corresponding author. Tel.: +1 213 821 2034; fax: +1 213 740 1056.
E-mail address: malmstad@usc.edu (N. Malmstadt).

http://dx.doi.org/10.1016/j.bbamem.2014.06.020
0005-2736/

reactions. For the general case of phospholipid membrane oxidation, molecular dynamics simulations of a 1,2-dioleoyl-sn-glycero-3-phosphocholine (DOPC) membrane reveal membrane bending and pore formation within nanoseconds of oxidation, especially with scission of both acyl tails [17]. Investigations adding photosensitizers to 1-palmitoyl-2-oleoyl-sn-glycero-3-phosphocholine (POPC) and DOPC GUVs reported changes to the membrane bending modulus [18] and area expansion modulus [19] with lipid oxidation. Others observed increases in the membrane surface area accompanied by vesicle shape fluctuations when irradiating porphyrin-labeled pure POPC or POPC-containing GUVs [16,20]. In addition, a study using DOPC GUVs in different concentrations of methylene blue solution also observed post-expansion membrane area contraction accompanied by the loss of optical contrast across the membrane; this was interpreted as the result of pore formation [21]. Similar effects have also been reported in polymersomes composed of polyethyleneoxide-*b*-polybutadiene (PEO-*b*-PBD) diblock copolymer with the chromophore chlorin e6, where the vesicles grew larger over three minutes and also shrunk afterwards [22]. In this study, the morphological changes previously observed by others are utilized to constructing a kinetic model of oxidation progress. This modeling approach provides a generalizable framework for quantifying and predicting the results of photosensitization-induced oxidation processes. Additionally, this work provides the first visual confirmation of micron-sized pore formation accompanying vesicle shrinkage in the latter stage of oxidation. We show that careful observation of pore dynamics can be used to estimate changes in the line tension of the membrane.

A baseline understanding of the dynamics of lipid oxidation is of broad utility. Rhodamine-based dyes are broadly used in imaging studies; understanding the precise conditions under which they can be expected to lead to oxidative damage–and potential artifactual results–is therefore important. Rhodamine dyes have also been considered as potential photosensitizers in photodynamic therapy (PDT) [11,23]. Understanding the kinetics of oxidation produced by the photosensitizer is the key to designing such therapies, and the framework of our kinetic model is extensible beyond rhodamine fluorophores to other photosensitizers, such as porphyrin chromophores [24]. Despite many observations of light-induced oxidation of the lipid membrane, the dynamics of the underlying chemical events is largely unexplored, so the main goal of this study is to provide a kinetic model applicable to the complex process of oxidation while retaining simplicity by constraining to rate-limiting processes. Based on the morphological changes observed by others [16,20–22] and in this study, the process is apparently a two-step process involving membrane area expansion followed by contraction. Bateman and Gee [25] described the rate of light-induced oxidation of non-conjugated olefins to be first-order in which the effective rate constant varies proportionally with light absorption, which directed the focus of our study toward the dependence of oxidation dynamics on the intensity of the excitation light.

2. Materials and methods

2.1. Materials

The lipids 1,2-dioleoyl-sn-glycero-3-phosphocholine (DOPC), 1,2-dipalmitoyl-sn-glycero-3-phosphoethanolamine (DPPE), 1,2-diphytanoyl-sn-glycero-3-phosphocholine (DPhPC), and 1,2-dipalmitoyl-sn-glycero-3-phosphoethanolamine-N-(lissamine rhodamine B sulfonyl) (RhDPPE) were purchased from Avanti Polar Lipids. Sucrose, glycerol, 6-hydroxy-2,5,7,8-tetrametylchromane-2-carboxylic acid (Trolox), and 4-(2-hydroxyethyl)-1-piperazineethanesulfonic acid (HEPES) were purchased from Sigma-Aldrich. Glucose and Rhodamine B were purchased from Alfa Aesar, chloroform was from Macron Fine Chemicals, and sodium azide was from BDH Chemicals. Deuterated chloroform was from Cambridge Isotope Laboratories, Inc.

2.2. GUV preparations

Our standard GUV composition consisted of 9:1 molar ratios of DOPC to RhDPPE. In reducing DOPC concentrations to 85 and 75%, the unsaturated lipid was substituted with DPhPC such that RhDPPE was maintained at 10% of the total composition; DPhPC was selected as a substitute that would have a fluidity and phase behavior similar to that of an unsaturated lipid without susceptibility to oxidation. To investigate rhodamine content dependence, RhDPPE was substituted with unlabeled DPPE.

The GUVs were formed using the electroformation method pioneered by Angelova and coworkers [26]. A lipid solution (in chloroform) was deposited on an indium-tin oxide (ITO)-coated side of a glass slide (Delta Technologies), inside the perimeter enclosed by a silicone o-ring (13/16″ ID, 1″ OD, Sterling Seal & Supply) attached to the slide by silicone vacuum grease (Dow Corning). After drying under vacuum overnight, the lipid film was hydrated with a 200 mM sucrose solution in 10 mM HEPES buffer at pH 7.40 such that the final lipid concentration was 30–40 μg/mL. The electroformation apparatus was completed by attaching another ITO-coated slide to the o-ring with vacuum grease, with the conductive side facing toward the lipid film. Electrodes connecting each of the ITO-coated slides to a function generator (Hewlett–Packard/Agilent Technologies) allowed for the application of an AC field at 10 Hz and 1.3 V for 1 h at room temperature. Vesicles were used within a day of electroformation. Lipid mixtures containing rhodamine dye were always shielded from ambient light to avoid photobleaching and other unintended oxidation effects.

For dual-beam optical trap (DBOT) experiments, which require a higher density of GUVs in solution, GUVs were formed by hydrating the lipid film dried on a layer of agarose hydrogel [27–29]. The GUVs were formed in 500 mM sucrose solution in 20 mM HEPES buffer at pH 7.00, a condition used in the previous work with a DBOT [30,31].

2.3. Basic photooxidation experiments

Electroformed RhDPPE-labeled GUVs were observed with epifluorescence microscopy on a Nikon TI-E inverted microscope, using illumination filtered through a green excitation filter (528–553 nm bandpass, 540 nm cut-on wavelength). Excitation light was provided by a 130 W mercury lamp (Intensilight, Nikon). The maximum irradiation intensity through the objective (Apo TIRF 60× Oil/NA 1.49, Nikon) was measured by a laser power meter (Thorlabs, Inc.) to be 5.93 mW at 561 nm. Intensity was reduced in binary ratios using neutral density filters. We utilized asymmetry in aqueous solutions to facilitate microscopy observations: the GUVs formed in sucrose were transferred to an isoosmotic glucose solution (200 mM in 10 mM HEPES at pH 7.40). Since sucrose solutions are denser than glucose solutions at the same concentration, the GUVs sedimented to rest on the glass coverslip, minimizing their distances to the objective and their mobility. Figure S1 illustrates the described arrangement.

To estimate line tension in the pore-forming regime of DOPC GUV oxidation, pore closure was delayed by performing the experiments in ten-fold elevated aqueous viscosity. Both 200 mM glucose and sucrose solutions were formed in a 1:1 v/v glycerol–water mixture. The viscosity of the resulting sucrose solution was measured with an Ubbelohde viscometer (Cannon Instrument Company) to be 10.3 mPa·s.

2.4. Chemical analysis of oxidized lipids

In preparation for nuclear magnetic resonance (NMR) spectroscopy, lipid samples (in chloroform) were dried onto the bottom of a glass vial under an argon stream and placed under vacuum for at least 1 h. The samples were irradiated with the green excitation light for 1 h. Samples were redissolved in ~800 μL of deuterated chloroform and scanned on a Varian VNMRS-500 2-channel NMR spectrometer at 25 °C. Samples

were scanned prior to irradiation and after each of four subsequent cycles of green excitation light exposure.

2.5. Oxidation while stretching in a dual-beam optical trap (DBOT)

Rapid GUV fluctuation in early stages of oxidation made it difficult to accurately measure membrane surface area. For accurate area measurements, we repeated a set of the oxidation experiments while GUVs were captured and stretched in a dual-beam optical trap (DBOT). In a DBOT, counter-propagating laser beams emitted from two single mode optical fibers form a trap at the geometric center of the two fiber cores, owing to the Gaussian intensity profile of the beams [32,33], as illustrated in Fig. 2S. In our apparatus, described in detail elsewhere [31], the optical fibers are placed on grooves etched on silicon which ensure the fiber core alignment. Perpendicular to the fiber grooves runs another groove that houses the microfluidic glass channel. The GUVs were flowed through this glass channel using a peristaltic pump and were brought close to the trapping region. The vesicles were initially lifted to the center of the channel and trapped using a minimal laser power (50 mW from each fiber operating at a wavelength of 808 nm). At this point, we started capturing images of a GUV at the equatorial plane, using a CCD camera, through a 50× (NA 0.55, Nikon) objective at a frame rate of 62 fps. The rhodamine excitation light was emitted through the same objective, using the same green excitation filter described above but with a weaker illumination source (Nikon TE2-PS100W), in order to initiate the oxidation process. Maintaining the GUV in the trap, we then increased the laser power to 250 mW (from each laser) and caused the GUV membrane to stretch. The GUV was kept stretched for 5 s and the laser power then dropped to zero. Keeping the rhodamine excitation illumination on, the stretching experiment was repeated 15–20 times in order to capture data at several points over the course of oxidation.

2.6. Data analysis

The time-lapse image sequence observed by epifluorescence microscopy for the oxidation of each GUV was recorded by Nikon NIS Elements software in the ND2 file format, which was then imported into MATLAB for data processing using the Bio-Formats m-file package available through the University of Wisconsin-Madison Laboratory for Optical and Computational Instrumentation (LOCI). The GUV edge was traced using built-in MATLAB functions to apply a Gaussian filter and Canny edge detection. For images in which pores were evident, the portion of the GUV perimeter occupied by the pore was traced by fitting observable edge coordinates to an ellipse. With the knowledge of the coordinate of the vesicle center and the lengths of the major and minor axes, the angle of the arc from the dark void in the membrane was then used to calculate the arc chord corresponding to pore diameter.

At the quasi-static leak-out limit where pore radius and surface tension are assumed constant with respect to time, Karatekin and coworkers [34] simplified the hydrodynamic model of pore closure from a differential equation to the linear relationship

$$R^2 \ln r = -\frac{2\tau}{3\pi\eta_0} t + C \quad (1)$$

where R and r are the GUV and pore radii respectively and t denotes time. The aqueous viscosity is denoted by η_0, and C is a constant of integration. By plotting $R^2 \ln r$ as a function of time, the measured slope of the linear region was then used to calculate τ, the line tension. Fig. S4 shows an example of such plot, which reflects a sudden rise at pore opening, the linear decrease characteristic of the quasi-static leak-out regime, and a rapid drop toward pore closure.

In order to reproducibly and objectively select the linear region from the full pore closure data set, an adaptation of a truncation algorithm was used [35]. First, data points preceding the occurrence of the maximum pore radius as well as those showing total pore closure ($r = 0$) were removed. The remaining pore radii comprise data set A. Another data set consists of points from data set A, minus the end point. If the difference of the root mean squares (RMS) of the residuals from linear fittings of the two sets is equal to or exceeds 10% of the RMS of set A, then the removal of such point was considered to increase linearity. This step was iterated until the relative RMS change was less than 10% and/or there were fewer than four data points remaining. An example of an original and truncated data set is shown in Fig. S4.

In the case of the DBOT experiment, an in-house image-processing algorithm was applied in order to trace the GUV edge from the two-dimensional (2D) micrographs. The calculation of the three-dimensional (3D) vesicle surface area employed a method similar to one described by Milner and Safran [36]. The micrographs such as in Fig. S5b represent the equatorial cross-section of a stretched GUV having the ellipsoid shape. With data from the first time-point, the volume of this ellipsoid was approximated from the estimated major and minor axes of the cross-sectional ellipse, based on traced GUV (Fig. S5c) edge coordinates. The radius of the equivalent sphere (R) of the same volume was then obtained and used in the following equation:

$$r(\theta) = R + \left[\frac{1}{2}\left(3\cos^2\theta - 1\right)\right] u_2 \quad (2)$$

We assumed conserved volume of the GUV throughout the course of the experiment, so R is constant (note: DBOT experiments were terminated prior to the onset of pore formation). The second term represents the second-order Legendre polynomial associated with the gross shape change of the GUV under stretching tension. The 2D contours were fitted to Eq. (2) to relate the vesicle radius (r) as a function of the azimuthal angle (θ). Assuming the GUVs to be symmetric about the optical beam axis, we performed a solid angle of revolution integral on the fitted contour to obtain the surface area of the GUV.

3. Results and discussion

3.1. Time course of GUV deformation

The light-induced oxidation of DOPC GUVs is apparently a two-stage process: a typical example is shown in Fig. 1. GUVs are initially spherical and relaxed, with low-amplitude fluctuations observed (Fig. 1a). Within the first 3 min of irradiation, the vesicle flatten and expand out on the coverslip surface, resulting in an apparently greatly increased radius, and high-amplitude fluctuations are seen (Figs. 1b and 3b–e). As irradiation continues, the GUV returns to a rigid spherical shape (Fig. 1c), and micron-scale pores begin to regularly form (Fig. 1d–f). The two phases of decreased tension and flattening, followed by increased vesicle rigidity and membrane pore formation, can be seen clearly by plotting the apparent average radius of the GUV as a function of time (Fig. 1g). The radius plotted here represents the average radius of the traced vesicle contour (i.e. distance of the contour from the center point averaged across all angles) obtained by image analysis of epifluorescent micrographs. Note the initial rapid apparent vesicle size increase (flattening and fluctuations) to a peak radius followed by a decrease that is initially smooth but at long times becomes stepwise. Each step here corresponds to a single pore formation event releasing a fraction of the enclosed liquid and reducing the GUV volume. The time-course radius changes for other experimental conditions (varying excitation light intensity, DOPC concentration, and RhDPPE concentration) are available in Fig. S6.

Prior to membrane pore formation, the volume of the aqueous solution enclosed by the GUV membrane is assumed to be constant. Therefore, vesicle flattening leading to increased apparent vesicle radius is attributed to total membrane area expansion due to increased lateral molecular area from oxidation. Conversely, increased vesicle rigidity and pore formation are regarded as resulting from chemical changes to the lipid molecules with further oxidation, which led to decreased

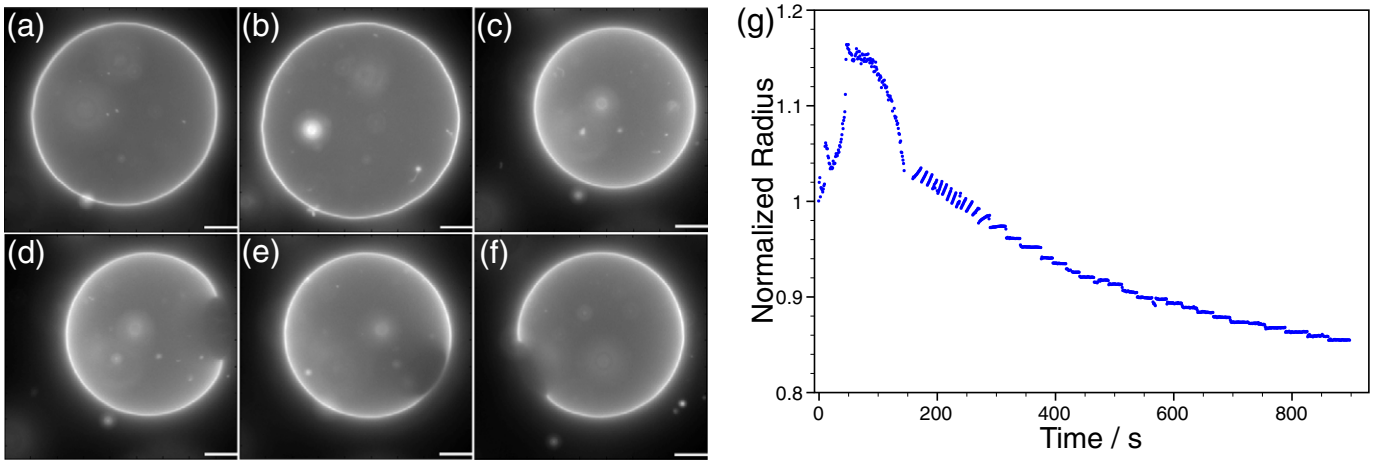

Fig. 1. Vesicle morphologies and radius profile during GUV oxidation at 0.72 mW rhodamine excitation intensity and 90 mol% DOPC–10 mol% RhDPPE. The epifluorescence micrographs in (a)–(f) show the same GUV (a) at the beginning of irradiation at 0 s, (b) during area expansion at 63 s, and with increased rigidity with (c) continuous membrane at 216 s and with pores at (d) 217 s, (e) 243 s, and (f) 289 s. Scale bars = 10 μm. The radius values normalized to initial GUV radius over 900 s for another GUV from the same electroformation batch is shown in (g).

membrane area. Membrane pore opening in such isoosmotic condition and aqueous-viscosity environment are not typically resolvable, so those formed were likely due to decreased pore closure-promoting line tension. The complex and multistep reactions that took place are simplified into these two observable stages to be used to build a kinetic model for the progression of lipid oxidation.

As introduced earlier, the oxidation of unsaturated phospholipids results in the addition of the hydroperoxy group adjacent to the double bond on the acyl tail, following allylic hydrogen abstraction and carbon-centered radical formation [37]. The presence of this newly added functional group increases the lateral area in the membrane that the lipid molecule occupies. Collectively, this leads to membrane area increase that we observed and is represented by the data in the 0 to 175 s interval of Fig. 1g. Further oxidation results in acyl chain scission and loss of lipid material from the membrane [38,39], resulting in lipid area and membrane area contraction. The described oxidation steps are briefly summarized in Fig. 2a.

We analyzed the chemical transformation of DOPC upon photooxidation. A 10 mol% mixture of Rhodamine B and DOPC was probed by ^{1}H NMR and successively oxidized as a thin film. The Rhodamine B signal did not interfere with the DOPC signal. We observed the evolution of three non-native DOPC peaks that are attributed to hydroperoxy, alcohol, and aldehyde groups (Fig. 2b). Singlet oxygen reacts with the olefin in the DOPC tail according to standard "ene" chemistry. In a concerted reaction, singlet oxygen reacts with an allylic hydrogen (with respect to the double bond) and a hydroperoxy group adds to the tail, shifting the double bond [40–42]. The hydroperoxy peak appears in the spectra after the first round of oxidation at around 4.4 ppm. Subsequent reduction of the hydroperoxide results in the formation of an alcohol. Finally the allylic alcohol undergoes a Hock rearrangement and the tail cleaves, resulting in an alcohol (4.25 ppm) and an aldehyde (9.75 ppm). In the end, the alcohol is converted to an aldehyde [10,43,44]. These aldehydes are present after the third round of oxidation. The head group was chemically stable as indicated in the consistency of spectra for all rounds of photooxidation in the 0.7–3.45 ppm range (Fig. S14). The control sample, which underwent the same drying and scanning protocol, did not exhibit any of the oxidation products.

To better understand the kinetics of these chemical transformations, we analyzed data produced by photooxidation experiments with GUVs: time series of images showing changing morphology (compare Fig. 1a–f). The molecular parameter that changes with the progress of oxidation is the area per lipid, so we needed to first measure vesicle surface area from each of these images in order to model the kinetics. In measuring surface area from these two-dimensional micrographs, we utilized image processing in MATLAB for membrane edge detection. The coordinates of the pixels comprising the vesicle edge were averaged to approximate the coordinates of the vesicle center, and the distances from the center to all edge points were then averaged to yield vesicle radius. We assumed that the GUVs were always spherical in calculating vesicle surface area from this radius.

In observation of GUVs resting on the coverslip surface, several experimental artifacts persisted and increased the uncertainty of the time course data during the membrane area expansion phase of oxidation when the vesicle morphology significantly deviated from a spherical shape. With flattened GUVs, as seen in Fig. 1b, the measured vesicle dimensions were overestimated, and adding high amplitude fluctuations (Fig. 3b) meant that the average radius data could not be used to accurately estimate changes in the membrane area that resulted in decreased tension. Furthermore, the GUVs mitigated increased surface area-to-volume ratios by storing excess membrane as tubules and buds, and these were later stretched out as further oxidation resulted in products with decreased surface area.

While the morphological transitions of GUVs are more accurately represented by Fig. 1, a few which formed tubules and buds to mitigate increased surface area (Fig. 3) experienced several brief interruptions during the membrane area-decrease phase. First, the surface tension of the flattened GUVs increased, as indicated by the return of the spherical shape (Fig. 3f). Excess membrane stored away as tubules was pulled back to the main GUV body and the sudden increase of membrane area was accompanied by more fluctuations (Fig. 3g). The time course radius data reflect this competition between the increasing membrane tension above the threshold necessary for spontaneous pore formation and the returning of excess membrane with cyclic rapid increase and step-decreases around 200 s in Fig. 1g. It should also be noted that the flattening and swelling of GUVs occurred rapidly and were not always accurately followed during epifluorescence microscopy so images were sometimes out of focus during these transitions. For the purpose of fitting the kinetic model, the data points representing these behaviors were not considered.

3.2. DBOT stretching results

Since the surface area of GUVs flattened on the glass surface cannot be accurately measured, oxidation experiments were repeated in a DBOT, which stretches the vesicles to allow accurate surface area measurements. We observed both the time at which peak area was achieved and the maximum area increase at this peak. The distributions of peak time and maximum area strain, confirmed to be normal by the

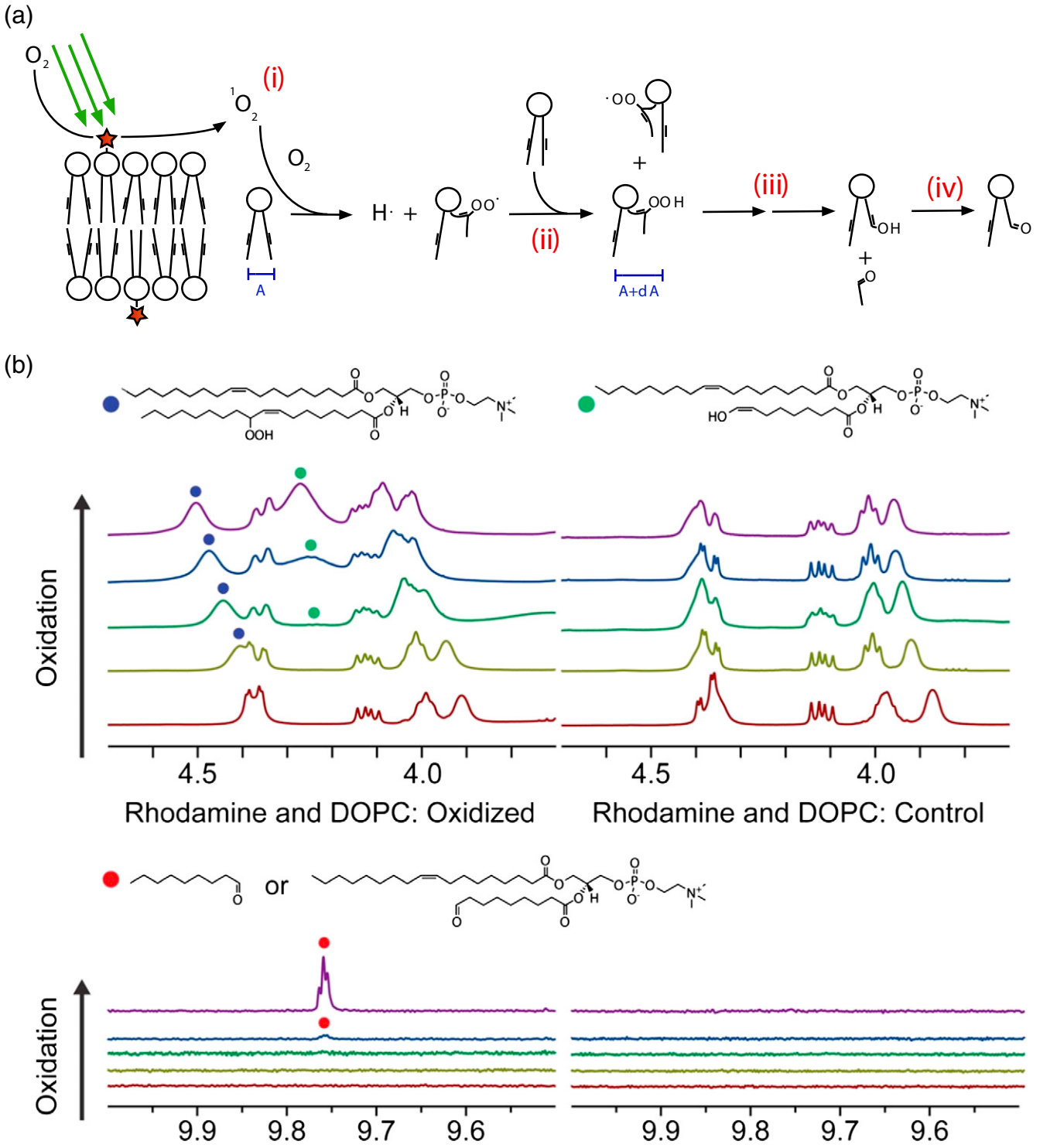

Fig. 2. (a) The mechanism of photo-induced oxidation. (i) The allylic hydrogen is abstracted by $^1O_2$ and with the addition of molecular oxygen, the peroxyl radical is added in its place. (ii) The peroxyl radical can initiate the oxidation of neighboring lipid molecules to result in a hydroperoxy (–OOH) group adjacent to the double bond. (iii) Oxidation of the –OOH group results in lipid tail scission into a shortened acyl chain capped with a hydroxyl (–OH) group and a tail fragment capped with the aldehyde (–CHO) group. (iv) Further oxidation of –OH on the shortened lipid molecule results in its replacement with –CHO. (b) ^{1}H NMR spectra of oxidized (left) and non-oxidized (right) samples of 90%DOPC–10%Rhodamine B. The colored dots indicate the oxidation products: (blue) hydroperoxy, (green) alcohol, and (red) aldehyde. The bottom spectra are of stock samples and each successive spectrum was taken after a cycle of evaporating chloroform (both oxidized and control), irradiating to excite Rhodamine B for 1 h (oxidized batch only), and redissolving in deuterated chloroform for ^{1}H NMR spectroscopy (both oxidized and control).

Kolmogorov–Smirnov test, are summarized in Fig. 4. The formation of membrane tubules led to multiple peaks in the time-course measurement of vesicle size (Fig. S9); the vesicles that exhibit such behavior were excluded from the distribution of the maximum percent area increase (Fig. 4b).

The GUV membrane area increased by 7.81 ± 2.75% on the DBOT apparatus. Note that the light source used was significantly weaker than that used in the main setup, as shown by the lengthened time to maximum area increase (Fig. 4a). Mertins and coworkers reported that the maximum area increase depends on the rate of singlet oxygen

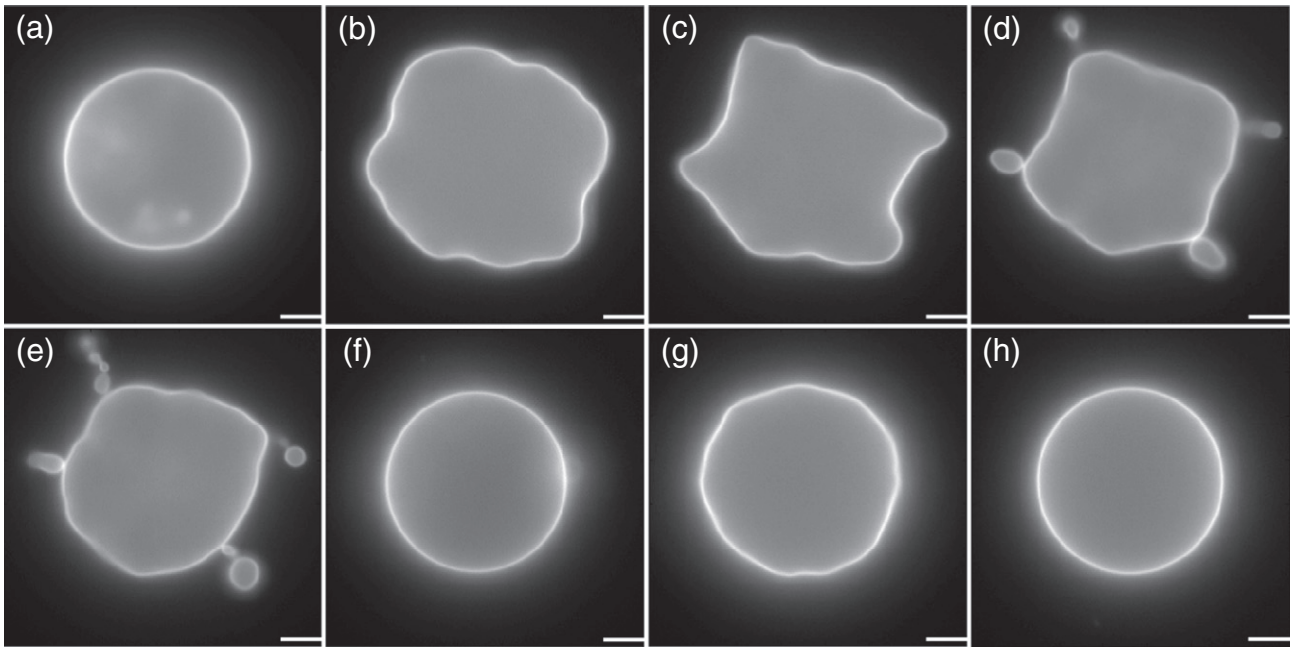

Fig. 3. Area storing morphologies during oxidation of a 90 mol% DOPC–10 mol% RhDPPE GUV irradiated at 0.72 mW rhodamine excitation intensity from (a) the beginning of irradiation at 0 s. The GUV underwent the area expansion phase of oxidation and formed tubules and connected buds from (b) 51 s, (c) 55 s, (d) 61 s, and (e) 71 s. During the transition phase, the GUV membrane area was reduced and rigidity increased at (f) 169 s before increased surface tension stretched a tubule and returned excess membrane area at (g) 177 s. The GUV became fully rigid by (h) 207 s. Scale bars = 10 μm.

formation [21], which can be controlled by changing photosensitizer concentration and irradiation intensity. The time-course surface area calculations based on data collected with the DBOT apparatus were also used for fitting to the dynamical model described next.

3.3. Modeling oxidation kinetics

Based on the two distinct stages of oxidation observed, we modeled DOPC oxidation as having two rate-limiting steps in series; each step was simplified to an irreversible reaction with one collective species each for reactant and product. The product of the first reaction is an oxidized species (called OX1) that occupies more membrane area than non-oxidized DOPC does. The product of the second reaction is called OX2, which occupies less area than DOPC. Bateman and Gee [25] observed that the kinetics of photochemical oxidation of non-conjugated olefins have first-order dependence on the concentration of the species to be oxidized. We therefore assume first-order kinetics for both steps. The dependence of reaction rate on illumination intensity will be taken into account via modifications of the effective rate constant of both reactions, which are

$$\mathrm{DOPC} \xrightarrow{k_1} \mathrm{OX1},\quad r_1 = k_1 C_{\mathrm{DOPC}} \tag{3a}$$

$$\mathrm{OX1} \xrightarrow{k_2} \mathrm{OX2},\quad r_2 = k_2 C_{\mathrm{OX1}} \tag{3b}$$

where k_1 and k_2 are the rate constants for the first and second steps, respectively, and r_1 and r_2 are the reaction rates. The material balances for the three species are

$$\frac{dC_{\mathrm{DOPC}}}{dt} = -k_1 C_{\mathrm{DOPC}} \tag{4a}$$

$$\frac{dC_{OX1}}{dt} = k_1 C_{DOPC} - k_2 C_{OX1} \tag{4b}$$

$$\frac{dC_{\mathrm{OX2}}}{dt} = k_2 C_{\mathrm{OX1}} \tag{4c}$$

Using the initial conditions

$$C_{\mathrm{DOPC}}(t=0) = 1 \tag{5a}$$

$$C_{\mathrm{OX1}}(t=0) = C_{\mathrm{OX2}}(t=0) = 0. \tag{5b}$$

This system can be analytically solved in order to obtain expressions for the relative concentrations as a function of time (t), which are

$$C_{\mathrm{DOPC}}(t) = e^{-k_1 t} \tag{6a}$$

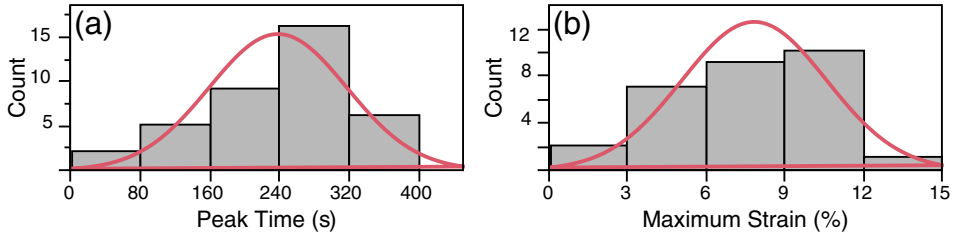

Fig. 4. Distribution of (a) time of irradiation (237.57 ± 79.80 s) at 0.313 mW (561 nm) to arrive at and (b) the percent increase (7.81 ± 2.75%) at the maximum membrane area increased due to lipid oxidation on the DBOT setup.

$$C_{OX1}(t) = \frac{k_1}{k_1 - k_2}\left(e^{-k_1 t} - e^{-k_2 t}\right) \quad (6b)$$

$$C_{OX2}(t) = 1 - \frac{k_2}{k_2 - k_1}e^{-k_1 t} + \frac{k_1}{k_2 - k_1}e^{-k_2 t}. \quad (6c)$$

We also assumed that the GUV surface area (S) is a simple linear combination of the surface areas of the three species (DOPC, OX1, and OX2)

$$S(t) = A_{DOPC}C_{DOPC}(t) + A_{OX1}C_{OX1}(t) + A_{OX2}C_{OX2}(t) \quad (7)$$

where A_{OX1} and A_{OX2} are the areas per lipid of OX1 and OX2, respectively, relative to that of DOPC, A_{DOPC} (i.e. $A_{DOPC} = 1$, $A_{OX1} > 1$, $A_{OX2} < 1$).

The rate constants (k_1 and k_2) and area parameters (A_{OX1} and A_{OX2}) were obtained through fitting the above model (Eq. (7)) to normalized area data averaged from approximately twenty GUVs for each experimental condition. Fig. 5 shows model results for 90%DOPC–10%RhDPPE GUVs irradiated at 2.85 mW over 15 min using epiflorescent microscopy during photooxidation without optical trapping. Note that the area expansion regime only spanned an interval of 80 s, and more time points were considered during this interval in which surface area changed rapidly.

Again using epifluorescent microscopy without optical trapping, we studied the same GUV composition (90 mol% DOPC–10 mol% RhDPPE) excited by five different power levels measured to be 2.85, 1.40, 0.72, 0.38, and 0.19 mW. Each condition was represented by time-course data averaged from approximately 20 GUVs. The four parameters in our kinetic model were obtained through least-squares minimization (described in the Supplementary information). The results of four fitting parameters are summarized below in Fig. 6. The kinetic expression given by Bateman and Gee [25] shows oxidation rate scales as the square root of light absorption. Since the rate of light absorption linearly varies with the incidental light intensity, we plotted the rate constants as a function of the square root of intensity and observed approximately linear behavior.

The area parameter A_{OX1} represents the relative area of the oxidized species resulting from the first rate-limiting step of DOPC oxidation, compared to the lateral area that a DOPC molecule occupies: 0.68 nm^2 [17]. To estimate this parameter, we averaged the best-fit value from experiments at various illumination intensities. Our estimate of the molecular area increase of oxidized DOPC at 16.9% is within the ranges reported by Weber (15–20%) [19] and predicted by molecular dynamics simulation [2].

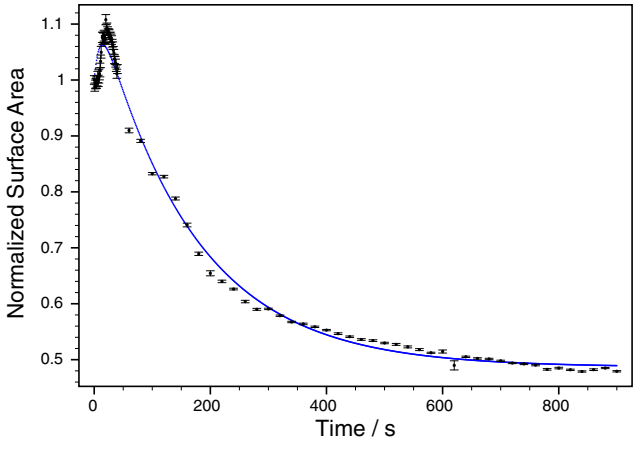

Fig. 5. Kinetic model (blue, solid line) fitted to data (black, dots) averaged from 20 GUVs of 90 mol% DOPC–10 mol% RhDPPE composition, irradiated at 2.85 mW for 15 min. Parameters obtained from this fit are $A_{OX1} = 1.1165 \pm 0.0148$, $A_{OX2} = 0.4867 \pm 0.0021$, $k_1 = 0.0977 \pm 0.0037\ s^{-1}$, and $k_2 = 0.0061 \pm 0.0001\ s^{-1}$.

Fig. 6a also depicts diminishing values of A_{OX2}, the relative area of the final oxidized species OX2, with higher irradiation intensity. During this second area-contracting regime, the GUVs assumed rigid spherical geometry and the area measurement artifacts associated with the first oxidation phase were eliminated. Smith and coworkers [39] demonstrated that lipid tail scission from oxidation resulted in the loss of lipid materials as fragments from the membrane into the aqueous environment. Additionally, the molecular dynamics simulation work of Cwiklik and Jungwirth [17] predicted micellization of the shortened oxidation products. These results support our finding, shown by the behavior of A_{OX2}, that increased irradiation intensity (and thus increasing singlet oxygen formation and lipid oxidation rates) causes a collective decrease in the membrane area resulting from the loss of lipid mass from the membrane.

The rate constants k_1 and k_2 were expected to vary directly with the square root of irradiation intensity, following the model by Bateman and Gee [25]. At the highest irradiation intensity, k_1 appears to not conform to this model. Note that k_1 is related to the shape of the area-expansion peak. The rapid onset of this peak at high irradiation intensities presents an observational challenge that may have yielded an inaccurate result. Extrapolating the value of k_1 at 2.85 mW based on the linear fit of the other four points yielded $k_1 = 0.0490\ s^{-1}$, which also resulted in a reasonable fit to the surface area time course data (Fig. S10). With accurate area measurement in the area-contraction regime, the results of k_2 more clearly display its linear dependence on $I^{1/2}$.

Despite maintaining constant irradiation intensity throughout the span of each 15-minute experiment, the first oxidation step (to OX1) took place more rapidly than when oxidizing from OX1 to OX2. This could be visualized in Fig. 1g and quantitatively confirmed by the difference between k_1 and k_2. The fact that k_1 is one order of magnitude higher than k_2 is largely due to the autocatalytic nature of the first phase, where the allylic hydrogen abstraction of one lipid molecule resulted in a radical that can initiate oxidation of neighboring lipid molecules in the membrane.

With increased accuracy in membrane area measurements, we were able to use the data collected with the DBOT apparatus for fitting to the dynamical model. However, the GUV surface area could only be calculated until the maximum surface area increase was reached. Without certainty on whether membrane pores formed any time afterwards, we could neither assume constant volume for surface area calculation nor maintain the optical contrast required for vesicle stretching. Thus, time-lapse data collection from the DBOT experiment was concluded once vesicle shrinkage was observed, and any analyzed data point beyond the time at maximum strain was disregarded. The model described in the first part of this section requires data spanning over both membrane expansion and contraction phases, so there were not enough data points collected with the DBOT apparatus to constrain a four-parameter fit. With the parameters shown in Fig. 6 for 0.19, 0.39, 0.73, and 1.4 mW intensities, we assumed linear dependence of A_{OX2} on the irradiation intensity and of k_1 and k_2 on the square root of the intensity to extrapolate these three parameters for the irradiation intensity used in the DBOT experiments. Due to differences in light sources and microscope objective specifications between the basic setup shown in Fig. S1 and in the DBOT setup, this irradiation intensity (0.02 mW) was estimated by extrapolation from the linear fit as a function of the natural logarithm of time at the maximum area increase on the basic experimental setup, shown in Fig. S11. Aside from fixing the parameters A_{ox2}, k_1, and k_2, the data fitting protocol was identical to that for the basic oxidation experiment data. The resulting one-parameter fit of the kinetic model to the DBOT data yielded A_{OX1} of 1.1076 ± 0.0272; the distribution of A_{OX1} is shown in Fig. 7. We have acknowledged that the data from the basic experimental apparatus resulted in overestimated values of GUV surface area, so it is reasonable that the DBOT data would suggest a 10.7% increase in lipid area, which is less than the value obtained from the basic experiment data of 16.9%. However, this value is less than the

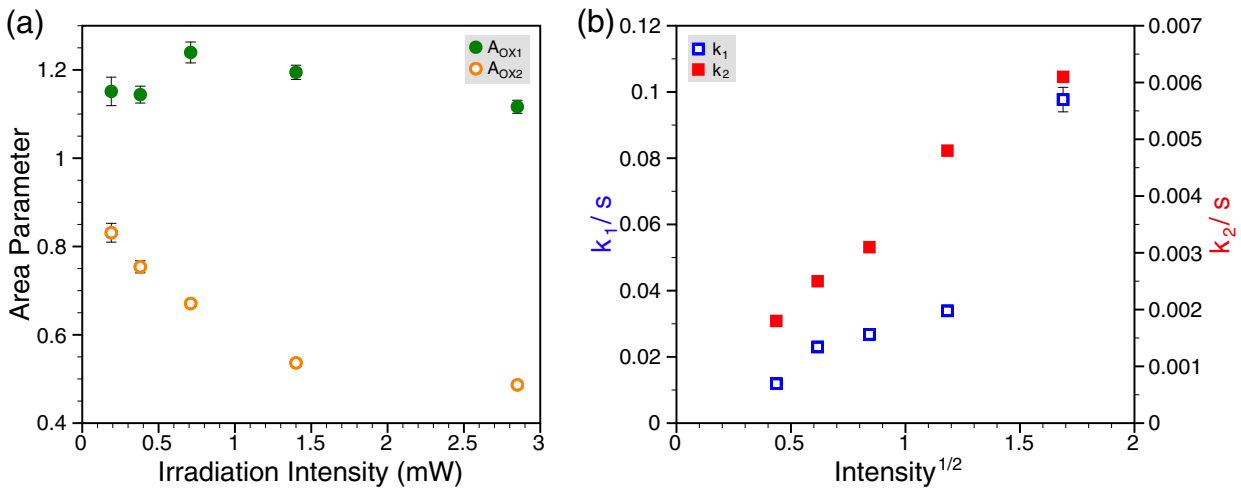

Fig. 6. (a) Area parameters A_{OX1} (green, filled circles) and A_{OX2} (orange, opened circles) as functions of the irradiation intensity (I) and (b) rate constants k_1 (blue, opened squares) and k_2 (red, filled squares) as functions of $I^{1/2}$, obtained through fitting the kinetic model to vesicle area time-course data averaged from ~20 90 mol% DOPC–10 mol% RhDPPE GUVs. Note that some error bars are smaller than the markers and are not visible.

lower limit of the ranges reported by Weber and predicted by Wong-Ekkabut [2,19].

3.4. Line tension of oxidized membrane pores

In addition to vesicle surface area changes, the excitation of the fluorescent dye labeling the phospholipid bilayer also resulted in experimentally observed pores in the membrane (Fig. 1d–f), such as those seen by Sandre and coworkers [45]. Pores often form at tensions beyond a certain threshold; above this threshold, vesicle membrane stress is mitigated by the ejection of liquid through pores. Energetically, pore opening competes with the line tension that arises from the energetic cost to arrange lipid molecules at the pore edge, that is why lipid pores are often small and short-lived and are not typically visible in standard microscopy experiments [45].

Sandre and coworkers [45] were able to observe pores by prolonging their durations. They formed GUVs in a mixture of water and glycerol, increasing the viscosity to 32.1 ± 0.4 mPa·s and slowing down the leakage process to delay pore closure. The pores formed could be resolved by optical microscopy and remained opened for seconds. Another way pore duration can be modified is altering membrane line tension by adding molecules with non-zero spontaneous curvatures. Surfactants and phospholipids with relatively large head groups can more easily be organized at the pore edge than those cylindrical lipids can. Treatment of DOPC GUVs with the surfactant triton X-100 resulted in pores that could last tens of seconds [46]. The opposite effect is observed for cholesterol, which has an inverse-cone shape [47].

Using glycerol to raise the viscosity of the aqueous phase ten-fold to 10.3 mPa·s, we increased the duration of pore opening from less than a second to 3–4 s, giving us 20–40 frames of epifluorescent micrographs

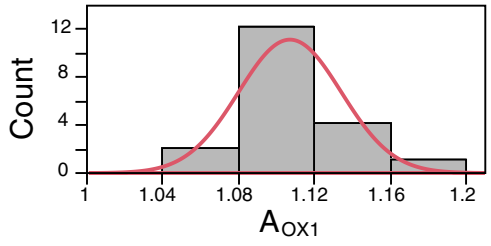

Fig. 7. The distribution of A_{OX1} obtained through fitting the kinetic model to the DBOT data of 19 90 mol% DOPC–10 mol% RhDPPE GUVs irradiated at an estimated intensity of 0.02 mW (561 nm); the Kolmogorov–Smirnov test confirmed normal distribution of the values averaged at 1.1076 ± 0.0272.

for each pore occurrence. We observed pore formation for three different compositions of decreasing DOPC concentration. As DOPC concentration decreased from 90% to 68%, membrane line tension increased from ~6 pN to ~10 pN and pore occurrence became less frequent with shorter duration. Karatekin and coworkers [34] also observed pores during prolonged illumination of fluorescently labeled DOPC GUVs, with measured line tension of 8.1 pN; the connection to lipid oxidation had not been made in this earlier work. In comparison, the line tension of non-oxidized DOPC membranes was estimated with electroporation experiments to be between 25 and 27 pN [48,49]. This indicates that a DOPC oxidation product resulting from lipid tail scission during the membrane-contracting phase decreases membrane line tension. This result suggests that these lipid products have edge-stabilizing inverse-cone geometry. The distributions, confirmed to be normal by the Kolmogorov–Smirnov test, of the line tension values for all three conditions are summarized in Fig. 8.

Smith and coworkers [39] studied lipid tail scission with oxidation and demonstrated that some tail fragments were lost to the aqueous environment. This is depicted in our study by shrinking GUV size following initial membrane-expansion. The contribution of lipid oxidation toward pore formation is two-fold. First, the decreasing vesicle membrane area encompassing an incompressible fluid accumulates surface tension required to drive pore opening. Second, the shortened lipid oxidation products were shown by us to reduce line tension with a pore edge-stabilizing geometry. Surface tension promotes pore formation while line tension acts against it, and lipid membrane oxidation alters both properties in favor of pore opening. In cells, increased membrane permeability due to pores then leads to solute imbalances triggering cell death [50].

3.5. Controlling for oxidation with sodium azide and Trolox

To demonstrate that oxidation was due to singlet oxygen, we performed the basic photooxidation experiment described in Section 2.3 in the presence of sodium azide, a specific quencher for singlet oxygen [51], and of Trolox, which scavenges free radicals [52]. With 1 mM Trolox present in the glucose solution outside the 90 mol% DOPC–10 mol% RhDPPE GUV, irradiation with green excitation light at 0.72 mW resulted in the same vesicle morphologies as in the condition without Trolox (Fig. S12).

The addition of 20 mM sodium azide yielded more interesting results. The presence of sodium azide induced vesicle adhesions, as shown in Fig. S13a. During the course of irradiation for photosensitization of the rhodamine dye, the GUV membrane area did not increase

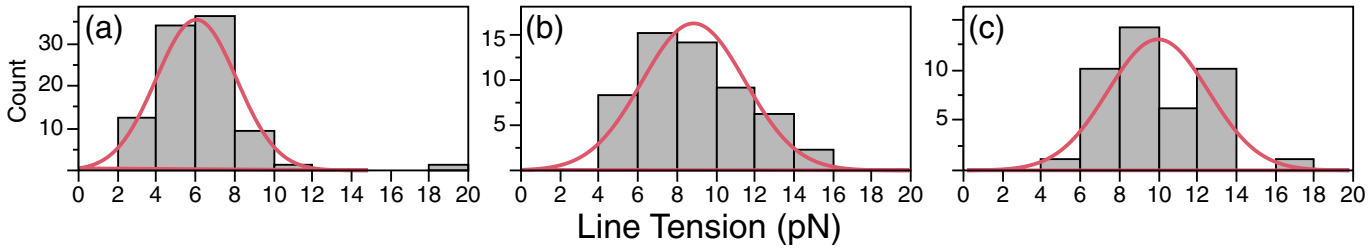

Fig. 8. Distribution of measured line tension values (pN) for (a) pure DOPC (6.10 ± 2.08 pN, n = 93), (b) 7:1 DOPC/DPhPC (8.89 ± 2.66 pN, n = 54), and (c) 3:1 DOPC/DPhPC (9.95 ± 2.56 pN, n = 42) GUVs, all with 10 mol% RhDPPE, in 1:1 v/v 200 mM sucrose solution/glycerol μ = 10.3 mPa·s).

but the vesicles eventually became smaller, as seen in the comparison between six GUVs in Fig. S13. We speculated that azide ions were gradually depleted during the 15 min of irradiation, as seen by restored vesicle mobility and separation (Fig. S13b), so milder lipid oxidation did occur. Nevertheless, as sodium azide specifically quenches singlet oxygen, this control experiment demonstrated that this ROS, formed through photosensitization, was in fact responsible for the oxidation of DOPC lipid molecules.

4. Conclusion

We demonstrated that the complex and multistep chemical processes of lipid oxidation could be simplified to rate-limiting steps in the formation of quasi-stable oxidation products, in order to follow the depletion of the original unsaturated lipid species without taking any chemical measurements. This kinetic model can be used as a tool for estimating the lateral molecular area of the resulting oxidation products, as well as the rate constants of the steps to form them. Applications beyond the fundamental studies may extend to fine-tuning the designs of photodynamic therapy treatments and controlled drug delivery vehicles through controlled lipid membrane deterioration with oxidation.

Acknowledgements

S.S. was supported in part by the University of Southern California Viterbi Dean's Doctoral Fellowship. This work was funded by the Office of Naval Research (Young Investigator Award #N000141310693). Methods for calculating the force on a GUV in a DBOT were funded by an NSF CAREER award under Grant. No. 0846143.

Appendix A. Supplementary data

Supplementary data to this article can be found online at http://dx.doi.org/10.1016/j.bbamem.2014.06.020.

References

[1] A.A. Spector, M.A. Yorek, Membrane lipid composition and cellular function, J. Lipid Res. 26 (1985) 1015–1035.
[2] J. Wong-Ekkabut, Z. Xu, W. Triampo, I.M. Tang, D.P. Tieleman, L. Monticelli, Effect of lipid peroxidation on the properties of lipid bilayers: a molecular dynamics study, Biophys. J. 93 (2007) 4225–4236.
[3] F. Cai, Y.M. Dupertuis, C. Pichard, Role of polyunsaturated fatty acids and lipid peroxidation on colorectal cancer risk and treatments, Curr. Opin. Clin. Nutr. Metab. Care 15 (2012) 99–106.
[4] P. Cejas, E. Casado, C. Belda-Iniesta, J. De Castro, E. Espinosa, A. Redondo, M. Sereno, M.A. Garcia-Cabezas, J.A.F. Vara, A. Dominguez-Cáceres, R. Perona, M. González-Barón, Implications of oxidative stress and cell membrane lipid peroxidation in human cancer (Spain), Cancer Causes Control 15 (2004) 707–719.
[5] J.M. Upston, X.W. Niu, A.J. Brown, R. Mashima, H.J. Wang, R. Senthilmohan, A.J. Kettle, R.T. Dean, R. Stocker, Disease stage-dependent accumulation of lipid and protein oxidation products in human atherosclerosis, Am. J. Pathol. 160 (2002) 701–710.
[6] D.A. Butterfield, C.M. Lauderback, Lipid peroxidation and protein oxidation in Alzheimer's disease brain: potential causes and consequences involving amyloid beta-peptide-associated free radical oxidative stress, Free Radic. Biol. Med. 32 (2002) 1050–1060.
[7] A. Reis, C.M. Spickett, Chemistry of phospholipid oxidation, Biochim. Biophys. Acta Biomembr. 1818 (2012) 2374–2387.
[8] A.W. Girotti, Mechanisms of lipid peroxidation, J. Free Radic. Biol. Med. 1 (1985) 87–95.
[9] B. Halliwell, J.M.C. Gutteridge, Oxygen toxicity, oxygen radicals, transition metals and disease, Biochem. J. 219 (1984) 1–14.
[10] C. Schneider, W.E. Boeglin, H.Y. Yin, D.F. Stec, D.L. Hachey, N.A. Porter, A.R. Brash, Synthesis of dihydroperoxides of linoleic and linolenic acids and studies on their transformation to 4-hydroperoxynonenal, Lipids 40 (2005) 1155–1162.
[11] R.C. Richmond, J.A. O'Hara, Effective photodynamic action by rhodamine 123 leading to photosensitized killing of Chinese hamster ovary cells in tissue culture and a proposed mechanism, Photochem. Photobiol. 57 (1993) 291–297.
[12] R. Rychtáriková, G. Kuncová, Immobilized singlet oxygen photosensitizers and their antimicrobial effect, Chem. List. 103 (2009) 800–813.
[13] D. Dolmans, D. Fukumura, R.K. Jain, Photodynamic therapy for cancer, Nat. Rev. Cancer 3 (2003) 380–387.
[14] J. Baier, T. Maisch, M. Maier, E. Engel, M. Landthaler, W. Bäumler, Singlet oxygen generation by UVA light exposure of endogenous photosensitizers, Biophys. J. 91 (2006) 1452–1459.
[15] A.G. Ayuyan, F.S. Cohen, Lipid peroxides promote large rafts: effects of excitation of probes in fluorescence microscopy and electrochemical reactions during vesicle formation, Biophys. J. 91 (2006) 2172–2183.
[16] C.K. Haluska, M.S. Baptista, A.U. Fernandes, A.P. Schroder, C.M. Marques, R. Itri, Photo-activated phase separation in giant vesicles made from different lipid mixtures, Biochim. Biophys. Acta Biomembr. 1818 (2012) 666–672.
[17] L. Cwiklik, P. Jungwirth, Massive oxidation of phospholipid membranes leads to pore creation and bilayer disintegration, Chem. Phys. Lett. 486 (2010) 99–103.
[18] H. Bouvrais, T. Pott, L.A. Bagatolli, J.H. Ipsen, P. Méléard, Impact of membrane-anchored fluorescent probes on the mechanical properties of lipid bilayers, Biochim. Biophys. Acta Biomembr. 1798 (2010) 1333–1337.
[19] G. Weber, T. Charitat, M.S. Baptista, A.F. Uchoa, C. Pavani, H.C. Junqueira, Y. Guo, V.A. Baulin, R. Itri, C.M. Marques, A.P. Schroder, Lipid oxidation induces structural changes in biomimetic membranes, Soft Matter 10 (2014) 4241–4247.
[20] K.A. Riske, T.P. Sudbrack, N.L. Archilha, A.F. Uchoa, A.P. Schroder, C.M. Marques, M.S. Baptista, R. Itri, Giant vesicles under oxidative stress induced by a membrane-anchored photosensitizer, Biophys. J. 97 (2009) 1362–1370.
[21] O. Mertins, I.O.L. Bacellar, F. Thalmann, C.M. Marques, M.S. Baptista, R. Itri, Physical damage on giant vesicles membrane as a result of methylene blue photoirradiation, Biophys. J. 106 (2014) 162–171.
[22] E. Mabrouk, S. Bonneau, L. Jia, D. Cuvelier, M.-H. Li, P. Nassoy, Photosensitization of polymer vesicles: a multistep chemical process deciphered by micropipette manipulation, Soft Matter 6 (2010) 4863–4875.
[23] C.R. Shea, N. Chen, J. Wimberly, T. Hasan, Rhodamine dyes as potential agents for photochemotherapy of cancer in human bladder carcinoma cells, Cancer Res. 49 (1989) 3961–3965.
[24] P. Morlière, R. Santus, M. Bazin, E. Kohen, V. Carillet, F. Bon, J. Rainasse, L. Dubertret, Is rhodamine 123 a photosensitizer? Photochem. Photobiol. 52 (1990) 703–710.
[25] L. Bateman, G. Gee, A kinetic investigation of the photochemical oxidation of certain non-conjugated olefins, Proc. R. Soc. Lond. A Math. Phys. Sci. 195 (1948) 376–391.
[26] M.I. Angelova, S. Soleau, P. Meleard, J.F. Faucon, P. Bothorel, Preparation of giant vesicles by external AC electric fields. Kinetics and applications, Progr. Colloid. Polym. Sci. 89 (1992) 127–131.
[27] J.S. Hansen, J.R. Thompson, C. Hélix-Nielsen, N. Malmstadt, Lipid directed intrinsic membrane protein segregation, J. Am. Chem. Soc. 135 (2013) 17294–17297.
[28] K.S. Horger, D.J. Estes, R. Capone, M. Mayer, Films of agarose enable rapid formation of giant liposomes in solutions of physiologic ionic strength, J. Am. Chem. Soc. 131 (2009) 1810–1819.
[29] N.L. Mora, J.S. Hansen, Y. Gao, A.A. Ronald, R. Kieltyka, N. Malmstadt, A. Kros, Preparation of size tunable giant vesicles from cross-linked dextran(ethylene glycol) hydrogels, Chem. Commun. 50 (2014) 1953–1955.
[30] M.E. Solmaz, R. Biswas, S. Sankhagowit, J.R. Thompson, C.A. Mejia, N. Malmstadt, M. L. Povinelli, Optical stretching of giant unilamellar vesicles with an integrated dual-beam optical trap, Biomed. Opt. Express 3 (2012) 2419–2427.
[31] M.E. Solmaz, S. Sankhagowit, R. Biswas, C.A. Mejia, M.L. Povinelli, N. Malmstadt, Optical stretching as a tool to investigate the mechanical properties of lipid bilayers, RSC Adv. 3 (2013) 16632–16638.
[32] J. Guck, R. Ananthakrishnan, H. Mahmood, T.J. Moon, C.C. Cunningham, J. Kas, The optical stretcher: a novel laser tool to micromanipulate cells, Biophys. J. 81 (2001) 767–784.

[33] B. Lincoln, S. Schinkinger, K. Travis, F. Wottawah, S. Ebert, F. Sauer, J. Guck, Reconfigurable microfluidic integration of a dual-beam laser trap with biomedical applications, Biomed. Microdevices 9 (2007) 703–710.
[34] E. Karatekin, O. Sandre, F. Brochard-Wyart, Transient pores in vesicles, Polym. Int. 52 (2003) 486–493.
[35] M.H. Kroll, K. Emancipator, D. Floering, D. Tholen, An algorithm for finding the linear region in a nonlinear data set, Comput. Biol. Med. 29 (1999) 289–301.
[36] S.T. Milner, S.A. Safran, Dynamic fluctuations of droplet microemulsions and vesicles, Phys. Rev. A 36 (1987) 4371–4379.
[37] A.W. Girotti, Lipid hydroperoxide generation, turnover, and effector action in biological systems, J. Lipid Res. 39 (1998) 1529–1542.
[38] N.A. Porter, S.E. Caldwell, K.A. Mills, Mechanisms of free-radical oxidation of unsaturated lipids, Lipids 30 (1995) 277–290.
[39] H.L. Smith, M.C. Howland, A.W. Szmodis, Q. Li, L.L. Daemen, A.N. Parikh, J. Majewski, Early stages of oxidative stress-induced membrane permeabilization: a neutron reflectometry study, J. Am. Chem. Soc. 131 (2009) 3631–3638.
[40] V.K. Ahluwalia, Oxidation in Organic Synthesis, CRC Press, Boca Raton, 2012.
[41] C.N. Skold, R.H. Schlessinger, The reaction of singlet oxygen with a simple thiophene, Tetrahedron Lett. 11 (1970) 791–794.
[42] E.N. Frankel, Lipid oxidation: mechanisms, products and biological significance, J. Am. Oil Chem. Soc. 61 (1984) 1908–1917.
[43] H.W. Gardner, R.D. Plattner, Linoleate hydroperoxides are cleaved heterolytically into aldehydes by a Lewis acid in aprotic solvent, Lipids 19 (1984) 294–299.
[44] H.H. Wasserman, R.W. Murray, Singlet Oxygen, Academic Press, New York, 1979.
[45] O. Sandre, L. Moreaux, F. Brochard-Wyart, Dynamics of transient pores in stretched vesicles, Proc. Natl. Acad. Sci. U. S. A. 96 (1999) 10591–10596.
[46] T. Hamada, Y. Hirabayashi, T. Ohta, M. Takagi, Rhythmic Pore Dynamics in a Shrinking Lipid Vesicle, Physical Review E, 80, 2009.
[47] E. Karatekin, O. Sandre, H. Guitouni, N. Borghi, P.H. Puech, F. Brochard-Wyart, Cascades of transient pores in giant vesicles: line tension and transport, Biophys. J. 84 (2003) 1734–1749.
[48] I. Genco, A. Gliozzi, A. Relini, M. Robello, E. Scalas, Electroporation in symmetrical and asymmetric membranes, Biochim. Biophys. Acta 1149 (1993) 10–18.
[49] T. Portet, R. Dimova, A new method for measuring edge tensions and stability of lipid bilayers: effect of membrane composition, Biophys. J. 99 (2010) 3264–3273.
[50] J.J. Lemasters, T.P. Theruvath, Z. Zhong, A.-L. Nieminen, Mitochondrial calcium and the permeability transition in cell death, Biochim. Biophys. Acta Bioenerg. 1787 (2009) 1395–1401.
[51] T. Maisch, J. Baier, B. Franz, M. Maier, M. Landthaler, R.-M. Szeimies, W. Bäumler, The role of singlet oxygen and oxygen concentration in photodynamic inactivation of bacteria, Proc. Natl. Acad. Sci. U. S. A. 104 (2007) 7223–7228.
[52] I.A. Castro, M.M. Rogero, R.M. Junqueira, M.M. Carrapeiro, Free radical scavenger and antioxidant capacity correlation of alpha-tocopherol and Trolox measured by three in vitro methodologies, Int. J. Food Sci. Nutr. 57 (2006) 75–82.